# Optimization of Fully Integrated Al Nanohole Array-Based Refractive Index Sensors for Use With a LED Light Source

Fritz Berkmann [ID], Lion Augel [ID], Michael Hack, Yuma Kawaguchi, David Weißhaupt [ID], Inga A. Fischer, and Jörg Schulze

*Abstract*—Plasmonic nanohole arrays that are directly structured into the top metallization of vertical Ge-on-Si PIN photodiodes can be used to sense refractive index changes. This concept can pave the way to fully integrated biosensors with small footprint and high sensitivities. Here, we show that by optimizing the layer structure of the Ge-on-Si PIN photodiode as well as the geometry of the nanohole arrays, we can achieve high and narrow optical responsivity peaks with Fano-resonance lineshapes. We used an iterative, simulation-based approach in order to optimize the photodiode layer structure as well as the nanohole geometry and compared the predictions to measurement results obtained from fabricated devices. Our fabricated device shows large peak shifts upon changes in the superstrate refractive index. Finally, we argue that the improved device setup can have potential applications in a sensor system that uses an LED light source and estimate the limit of detection to be $2.2 \cdot 10^{-5}$ RIU.

*Index Terms*—Biosensor, CMOS integration, nanohole-array, plasmonic, refractive index sensor.

## I. INTRODUCTION

**B**IOSENSORS based on detecting refractive index changes induced by analyte-ligand binding events have potential applications in a wide range of areas such as food safety and medical diagnostics. The possibility to use surface-plasmon polaritons at the interface between metals and dielectrics or localized plasmonic resonances in metallic nanoparticles for biosensors with high sensitivities is already well known [1] and an established technique in passive sensing devices

that require e.g., external spectrometers for read-out [2]–[5]. For many applications, however, a miniaturized on-chip approach in CMOS (Complementary metal-oxide-semiconductor) technology would be desirable. Here, closely integrating plasmonic structures with optoelectronic devices during their fabrication process can be a strategy to achieve a particularly small on-chip footprint for plasmonic refractive index sensors [6]–[9]. The integration of such sensors would enable the upscaling of the fabrication leading to a cost reduction per device. Also, the independence of an external read out electronic, which makes the commercially used detector in total rather bulky [10], is an important factor in terms of usability.

The sensitivity $S$ of a plasmonic sensor is defined by the shift of its resonance peak $\Delta\lambda_{\mathrm{peak}}$ initiated by a change in the surrounding – e.g., the superstrate above the sensor – refractive index $\Delta n_{\mathrm{sup}}$

$$S = \frac{\Delta\lambda_{\mathrm{peak}}}{\Delta n_{\mathrm{sup}}} . \tag{1}$$

The sharp and narrow plasmonic resonances helped to make these sensors a thriving field for research. Limitations in the integration arise from the reduction of sensitivity by bringing the plasmonic structures in contact with a substrate. In order to circumvent this issue the Al nanohole arrays (NHA) are integrated into the metallization of a Ge-on-Si PIN heterojunction photodiode. These devices can also be integrated into microfluidic systems [11]–[13]. The peak wavelength for extraordinary optical transmission (EOT) through the nanohole array at resonance is sensitive to changes in the superstrate refractive index and leads to sensitivities up to $\sim 1200$ nm/RIU for the measurement of bulk refractive index changes. With the optical transmission at resonance taking the shape of a Fano peak, the nanohole-array acts as a bandpass filter whose transmission peak can be shifted by the change of the superstrate refractive index. From a variation in device responsivities induced by the variation in transmission the change in the refractive index can be determined. Previously fabricated devices, however, exhibited rather broad responsivity peaks [13].

In this work we focus on reducing the width of the resonance of this type of sensor for potential application with an LED light source rather than a fixed-wavelength laser. Since LED light sources are cheaper than lasers and cover a wide wavelength
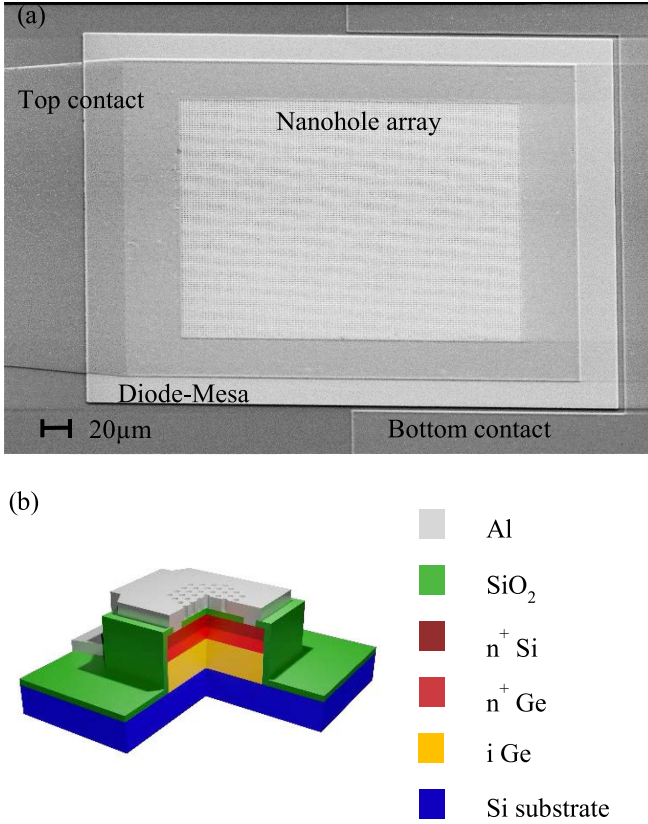
Fig. 1. SEM image (a) and three-dimensional model (b) of the fabricated Ge-on-Si PIN diodes with Al nanohole arrays as top metallization.

range, they are more like to be used in commercial approaches. To this end, we developed an iterative simulation-based optimization scheme and used the output as a basis for the fabrication of optimized devices (Fig. 1 shows an SEM image and a schematic cross-section of a device). Measurements of the fabricated sensors show the reduced spectral bandwidth of the sensor signal. We achieve good agreement with simulated peak positions even though the measured resonance is significantly broader than predicted by simulation. We estimate that it is possible to use these sensors for a commercial application that uses a LED as light source. Our results can serve as further steps towards on-chip integration of refractive index sensors with very small footprints.

## II. METHODS

For the simulation, we used the finite difference time domain (FDTD) solver of the ANSYS LUMERICAL software [14]. The diode was modelled as shown in the three-dimensional simulation model in Fig. 2. The boundary conditions were set to periodic boundary conditions (PBC) for the $x$ and $y$ directions to create the array. Perfectly matched layers (PML) were chosen in the $z$ direction. The angle of incidence of the plane wave was set normal to the surface. All materials were assumed to be perfectly smooth and defect free and no quantum effects were taken into account. To obtain the absorption inside the intrinsic Ge layer,

two transmission monitors were introduced at the interfaces of the intrinsic Ge layer. Based on the transmission monitor data, which gives the optical power normalized to the power of the incident wave, we calculated the responsivity as follows [15].

$$R = \frac{\frac{1}{2} \int \{\mathrm{Re}\,(S_{\mathrm{in}}) - \mathrm{Re}\,(S_{\mathrm{out}})\}\, dA}{\frac{hc}{\lambda}} \frac{q}{P_{\mathrm{source}}} \qquad (2)$$

Here, $S_{\mathrm{in}}$ and $S_{\mathrm{out}}$ are the Poynting vectors at the intrinsic Ge layer interfaces, $h$ is Planck's constant, $c$ is the speed of light in vacuum, $\lambda$ is the wavelength of incident light, $q$ is the elementary charge and $P_{\mathrm{source}}$ is the power of the plane wave.

Device responsivities were measured via a glass fiber based optical measurement setup consisting of a NKT SUPERK EXTREME supercontinuum laser, a NKT SUPERK SELECT acousto optical tunable filter (AOTF), an optical power meter (OPM) and a KEITHLEY 2636B source measurement unit (SMU). The photonic power is swept with a spectral step size of 5 nm in the range from 1200 nm to 1600 nm at 1.5 mW. During the measurement a beam splitter and an OPM were used to track the optical power. This was done to detect possible fluctuations of the optical power that would influence the calculation of the optical responsivity. The superstrate refractive index was adjusted by submerging the sample in different liquids. The glass fiber tip was also dipped into the superstrate liquid to avoid reflections on the liquid surface.

## III. SIMULATION-BASED OPTIMIZATION APPROACH

The device optimization scheme needs to consider different parameters assessing device performance. The peak responsivity should be as large as possible, the full width half maximum (FWHM) $\Gamma$ of the peak should be minimized and the sensitivity should be maximized. For practical approaches, operating the sensor at a fixed wavelength (or fixed wavelength range) would be most beneficial. Previously, the quantity $FOM^*$ has been introduced [16] to evaluate sensing performance at a fixed wavelength, which is defined with respect to the responsivity change $\Delta R_{\mathrm{opt}}$ measured for a superstrate refractive index change $\Delta n_{\mathrm{sup}}$ as

$$FOM^* = \max\left(\frac{\frac{\Delta R_{\mathrm{opt}}}{\Delta n_{\mathrm{sup}}}}{R_{\mathrm{opt}}}\Big|_{\lambda}\right). \qquad (3)$$

However, using this quantity as cost function for optimization is problematic since it favors low responsivities at the interrogation wavelength. Here, we therefore focus on a slightly modified quantity $FOM_n$ in order to select for a maximum signal change at a selected wavelength. We compared the change in the optical responsivity ($\Delta R_{\mathrm{opt}}$) introduced by the shift of the resonant peak to the change of the refractive index ($\Delta n_{\mathrm{sup}}$) to get a quantity that is sensitive to the relative signal change, i.e., the change in photocurrent.

$$FOM_n = \frac{\Delta R_{\mathrm{opt}}}{\Delta n_{\mathrm{sup}}} \qquad (4)$$
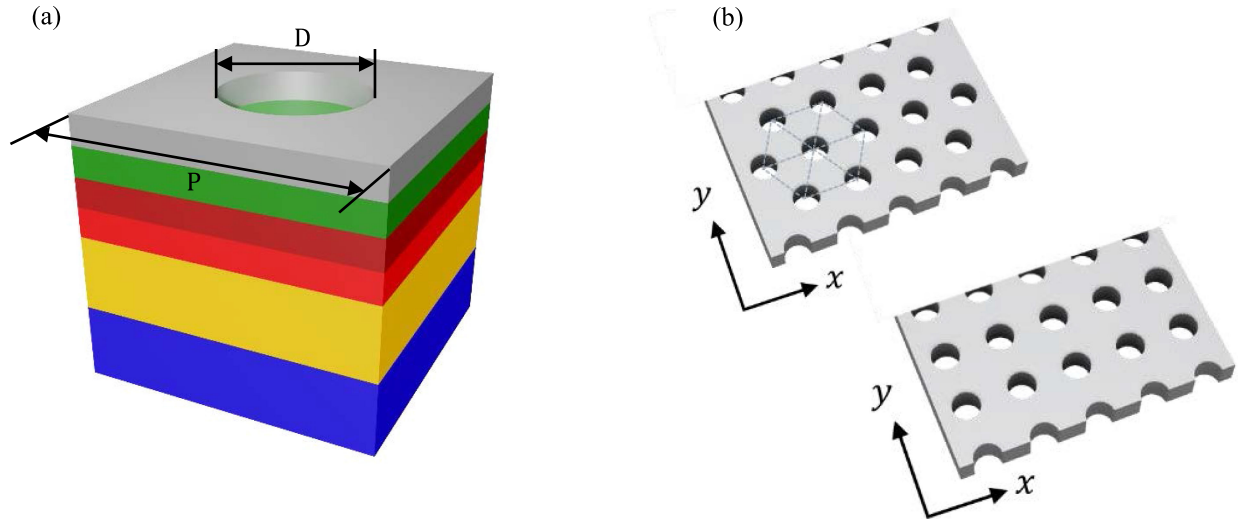
Fig. 2. (a) Three-dimensional unit cell model of the FDTD simulation and (b) the two different hole arrangements (square and hexagonal).
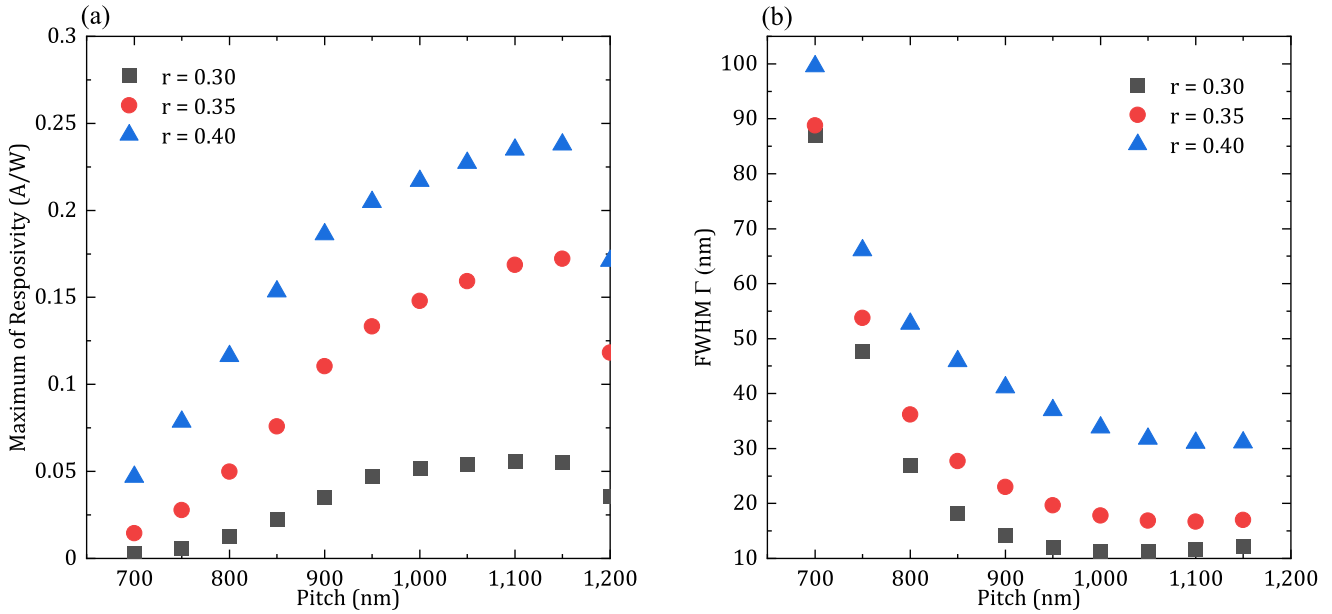


Fig. 3. (a) Maximum of responsivity $R_{\bigcirc max}$ and (b) FWHM $\Gamma_{\bigcirc}$ for a hexagonal nanohole array with a superstrate refractive index of n = 1.321 and layer thicknesses of t = 200 nm, $t_O$ = 50 nm and $t_{top}$ = 20 nm.

All geometry parameters, those pertaining to the structure of the diode as well as the geometry of the nanohole array [15], are potentially relevant to adjust sensor performance. While the geometry of the nanohole array has the strongest impact on the spectral position and the absolute responsivity of the responsivity peak, the thickness of all layers in the multilayer stack comprising not only the semiconductor layers but also passivation and metallization affects the resonance shape [15], [17]. Fig. 2 shows the 3D model of the simulation environment and the two different hole arrangements (square and hexagonal) of the Ge-on-Si PIN photodiode. By choosing a certain ratio r between the pitch P and the diameter D of the nanoholes, we can tune the optical responsivity as well as the FWHM of the responsivity peak as shown in Fig. 3.

Our investigations showed that it is not possible to optimize the thickness of the layers independently from each other or the chosen pitch diameter ratio. Therefore, the parameters, i.e., operation wavelength, ratio r, as well as the thicknesses of the Al, $SiO_2$ and Si/Ge hetero top contact layers, have to be optimized iteratively. The thickness of the intrinsic Ge layer was not optimized since its primary impact is to scale device responsivity. As a result, it has a negligible influence on the shape of the responsivity peak. Therefore it was set to a fixed value of 300 nm to facilitate the fabrication.

To find the optimal structure for our diodes as well as the geometry of the nanohole array we established an iterative top down/bottom up simulation approach. The starting point consisted of fixing a peak wavelength and a superstrate refractive
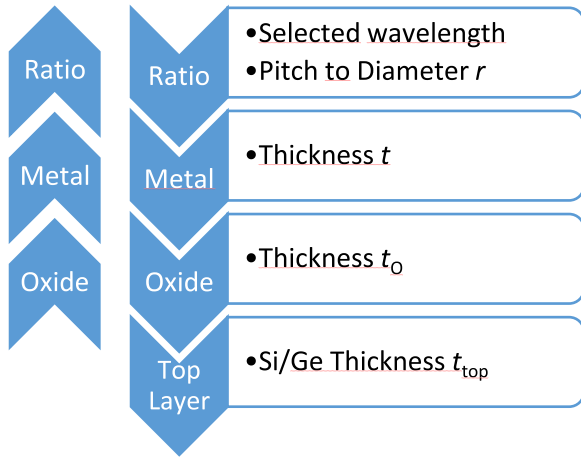
Fig. 4.    Workflow of the Simulative optimization.

index. As a next step, array pitch and hole diameter of the array were optimized, followed by the optimization of layer thicknesses of the Al metallization, the $SiO_2$ passivation and the Si/Ge hetero top contact. For the Si/Ge hetero top contactthe same layer thickness $t_{top}$ was chosen for the Si and the Ge layer to limit the number of optimization parameters. After having carried out these steps we selected a reverse approach and re-optimized the structure in a bottom up iteration step starting with the thickness of the Si/Ge hetero-top contact layer. With this approach, it is possible to choose a wavelength of operation and get an optimized nanohole array geometry as well as diode layer stack for the sensor. For different fields of application it is also possible to run the optimization for different superstrate refraction indices to fine tune the sensor i.e., for biosensing or gas sensing. Fig. 4 shows the workflow of the optimization.

One major advantage of this optimization scheme is its flexibility, i.e., it can be used for different combinations of targeted superstrate refractive index, readout wavelength and geometry. In order to demonstrate this, we carried out the optimization procedure not only for different nanohole array configurations but also for different superstrate refractive index ranges. The optimization was carried out for a square and a hexagonal nanohole arrangement targeted at two different potential fields of application. We chose a square (□) lattice arrangement optimized for a superstrate refractive index varying between $n = 1$ (air) and $n = 1.005$ at a fixed illumination wavelength of $\lambda = 1234$ nm (red line) for a potential application in the investigation of gaseous substances in air. A hexagonal (○) geometry was optimized for operation with a superstrate refractive index between $n = 1.321$ (deionized (DI) water) [18] and $n = 1.352$ (ethanol) [19] at a fixed illumination wavelength of $\lambda = 1295$ nm (red line) for the potential investigation of biofilms [20], [21].

## IV. DEVICE FABRICATION

Two different device types were fabricated, based on the separately optimized layer structures for the square NHA geometry and the hexagonal NHA geometry. The layers for the diodes were grown by molecular beam epitaxy (MBE) on a four-inch

$p^{++}$ Si (001) substrate. Before deposition the samples were cleaned using a thermal desorption step at a temperature $T = 900\,°C$ for five minutes. Afterwards a virtual substrate (VS) was deposited at $T = 330\,°C$ using a 100 nm thick intrinsic Ge layer. An in situ annealing step was performed at $T = 850\,°C$ for 300 seconds to decrease the threading dislocation density. On top of the VS an intrinsic Ge layer with a thickness of $d_{Ge-i} = 300$ nm was deposited at a substrate temperature $T = 330\,°C$. Subsequently, a Ge ($T = 250\,°C$) and a Si ($T = 330\,°C$) layer with thicknesses of d = 100 nm (□) and 40 nm (○) each and a Sb dopant concentration of $N_D = 10^{20}$ cm$^{-3}$ were deposited. The full layer structures are shown in the insets of Fig. 5.

Out of these samples, we fabricated vertical diodes with mesa sizes of $160 \times 160\,\mu m^2$. The layers were structured using optical lithography followed by a dry-etching step in an inductively coupled plasma reactive ion etching (ICP-RIE) system. After a cleaning step using $O_2$ plasma as well as Acetone and Isopropanol the diodes were covered with 190 nm (□) and 50 nm (○) of $SiO_2$ via plasma-enhanced chemical vapor deposition (PE-CVD) as passivation. Contact holes were structured into the passivation layer using optical lithography and a reactive ion etching system (RIE) as well as a wet-etching step with hydrofluoric acid (HF). After a second cleaning step, the Al layer was deposited via metal evaporation at a rate of 25 Å/s to achieve a smooth surface and afterwards structured via optical lithography and a dry-etching step in the ICP-RIE system. The structuring of the NHA happens simultaneously with the metal contact etching to avoid misalignment. To achieve the required lithography resolution for nanohole diameters below 500 nm we used AZ MIR-701 diluted with ethyl lactate (20:80).

## V. RESULTS AND DISCUSSION

Simulation results for the layer stack with optimized thicknesses as well as predicted device responsivities are shown in Fig. 5. The predicted resonance peaks are narrow with a FWHM of $\Gamma_{□} = 28.3$ nm, $\Gamma_{○} = 11.8$ nm, respectively and a maximum responsivity peak height of $R_{□max} = 0.08$ A/W, $R_{○max} = 0.17$ A/W, respectively. The asymmetry of the peak line shapes, which is more pronounced for the hexagonal nanohole array, is characteristic for Fano resonances. Remarkably, the peak responsivity predicted for the hexagonal nanohole array is more than twice as large as the peak responsivity predicted for the square nanohole array. The sensitivities predicted by simulation for the range of changes in superstrate refractive index investigated here are $S_{□} = 1200$ nm/RIU, $S_{○} = 967$ nm/RIU. The combination of these narrow peaks with high responsivities and sensitivities leads to a predicted $FOM_{□n} = 3.5$ A $\cdot$ W$^{-1}$ $\cdot$ RIU$^{-1}$ for the square arrangement as well as $FOM_{○n} = 5.5$ A $\cdot$ W$^{-1}$ $\cdot$ RIU$^{-1}$ for the hexagonal arrangement. Compared to previous work [13], were a FWHM of $\Gamma_{□} = 98$ nm and a sensitivity of $S_{□} = 967$ nm/RIU was predicted by simulation, our optimized structures show a clear reduction in linewidth. Strikingly, while the former work predicts a FOM* just above 100 for the square NHA, our simulation predicts a FOM* of 9026 for the hexagonal configuration. This strong increase is a result of a drastic decrease in the FWHM of the optimized structure. Our optimization approach
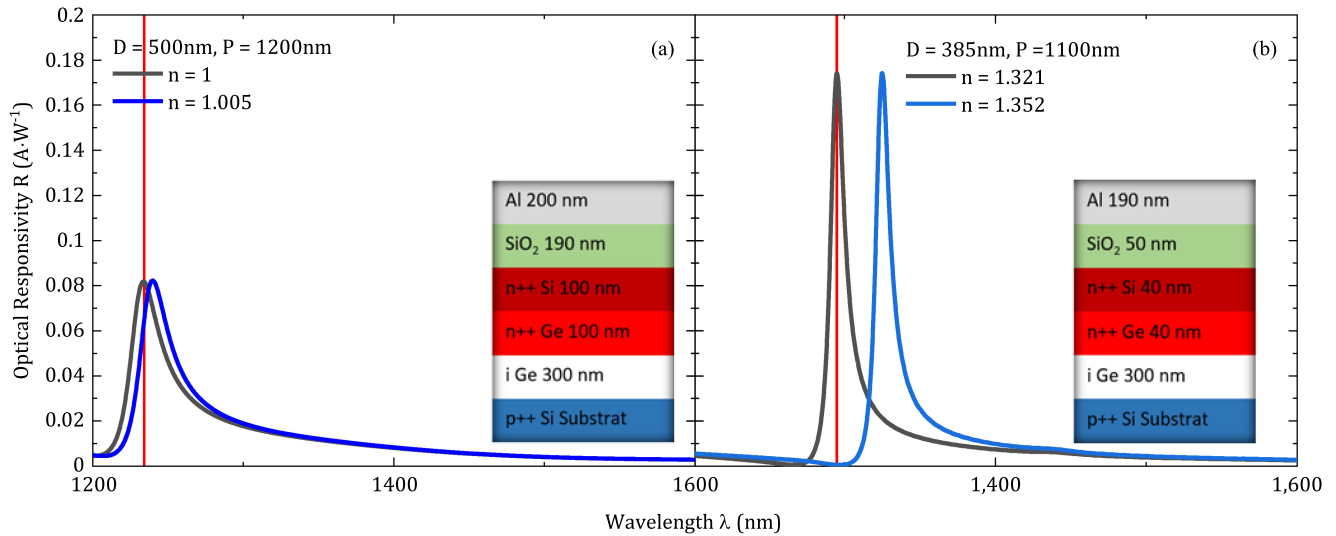
Fig. 5. Simulated optical responsivity for different (a: square and b: hexagonal) nanohole array arrangements as well as the optimized layer stacks and geometries. The red line marks the operating illumination wavelength.
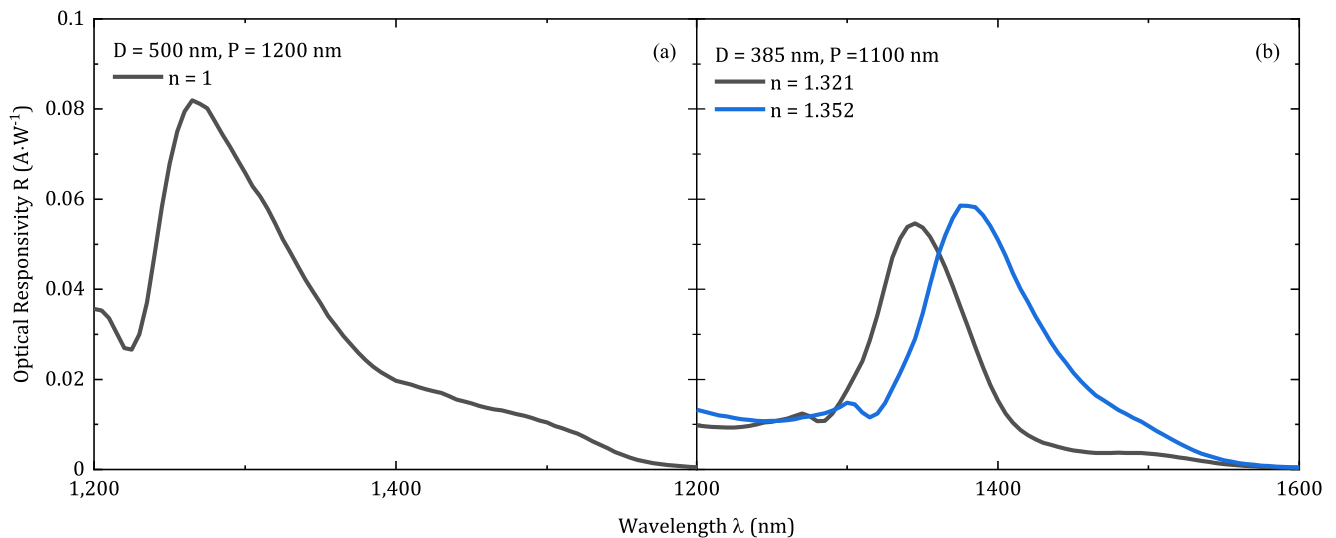


Fig. 6. Measured optical responsivity for different nanohole array arrangements (a: square and b: hexagonal).

TABLE I
COMPARISON BETWEEN SIMULATION AND MEASUREMENT RESULTS

| | | $\Gamma$ / nm | $R_{max}$ / A · W$^{-1}$ | $\lambda_{max}$ / nm | S / nm · RIU$^{-1}$ | FOMn / A·W$^{-1}$ · RIU$^{-1}$ | FOM* |
|---|---|---|---|---|---|---|---|
| □ | Simulation | 23.3 | 0.07 | 1234 | 1200 | 3.5 | 54.9 |
| | Measurement | 75.4 | 0.08 | 1265 | - | - | - |
| ⬡ | Simulation | 11.8 | 0.17 | 1295 | 967 | 5.5 | 9026 |
| | Measurement | 60.0 | 0.05 | 1345 | 967 | 0.83 | 36.8 |

leads to a predicted behavior of the simulated sensor that can potentially enable these sensors to work with a LED light source [22] rather than a laser.

The measured device responsivities also exhibit sharp responsivity peaks (Fig. 6) but are considerably broadened w.r.t.

simulation-based predictions. A detailed comparison can be found in Table I. For both devices, the measurements show a clear Rayleigh anomaly dip combined with a peak forming a sharp Fano resonance in the responsivity spectra. For the square arrangement we achieved a FWHM of $\Gamma_\square = 75.4$ nm (compared
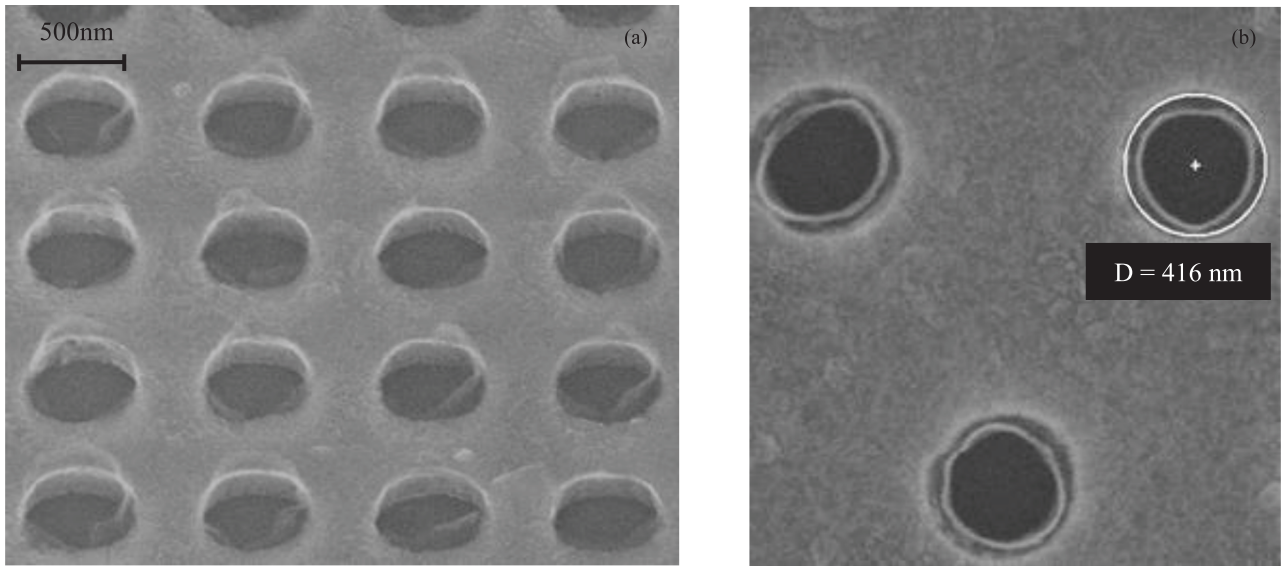
Fig. 7.    SEM images of the Nanohole arrays. Side view of the square (a) and top view of the hexagonal (b) arrangement.

to 23.3 nm predicted by simulation) with a relative peak height of $R_\square = 0.055$ A $\cdot$ W$^{-1}$. Due to the construction of the optical measurement setup, it was not possible to measure with other superstrate gases than air and the sensitivity of the square arrangement could not be measured in this experiment. However, our measurements show that our optimization decreases the FWHM in comparison to previous results [13], where a FWHM of 114 nm had been achieved.

For the hexagonal arrangement we obtain a FWHM of $\Gamma_\circ = 60.0$ nm with a relative peak height of $R_\circ = 0.044$ A $\cdot$ W$^{-1}$. Introducing a superstrate refractive index shift of $\Delta n = 0.031$ RIU leads to a peak position shift by $\Delta\lambda = 30$ nm and a measured sensitivity that is in very good agreement with a predicted sensitivity of $S_\circ = 967$ $nm \cdot RIU^{-1}$. Even though the FWHM is noticeably larger and the responsivity is smaller than predicted we were able to obtain FOM$_{\circ n}$ ($\lambda = 1345$ nm) = 0.83 A $\cdot$ W$^{-1} \cdot$ RIU$^{-1}$ as well as FOM$_\circ *(\lambda = 1385$ nm) = 36.8. The latter value is comparable to results achieved with gold nanorods and gold nanholarrays that were designed for biosensing [16], [23]. Comparing these results to previous work, where a maximum FOM$*$ of 16 was achieved [13], we note a pronounced improvement as a consequence of the reduced FWHM.

The comparison of the simulation results with the measurement results in Table I shows that the positions of the responsivity peaks are in good agreement. The measurements show a shift of the peak position of about 30 to 50 nm to higher wavelength and a lower shift of 15 to 20 nm for the Rayleigh dip compared with the simulations. There are a number of possible explanations for this shift such as a mismatch of the assumed Al permittivity data in the simulation and the permittivity of the Al deposited via evaporation, a difference in orientation of the polarization due to the measurement setup, or the formation of native aluminum oxide on the NHA. The roughness of the fabricated Al layer, for which RMS $=$ 5.854 nm was obtained from atomic force microscopy (AFM) measurements, originating e.g., from the

existence of metal grain boundaries can also contribute to the difference between simulation and measurements. Finally, a deviation in NHA geometry of the fabricated NHAs from the optimized configuration as determined by simulation can also strongly influence measurement results. Indeed, the diameter of the fabricated nanoholes was measured to be approximately 30 nm larger than the optimized value of 385 nm obtained from simulation. This is due to the lithography system whose native resolution is $> 500$ nm. These experimental imperfections can not only influence the positions of the resonance peaks but also their heights and widths. Furthermore, we also conjecture that the hexagonal nanohole geometry, while predicted to be superior as far as peak responsivity and resonance width are concerned, could be less robust w.r.t. fabrication imperfections than the square nanohole array.

Fig. 7 shows a SEM image of the fabricated NHAs. Besides the enlarged diameter, it can also be seen that the photoresist was not completely removed by the stripper, with residues around the holes visible both for the square and the hexagonal array. However, since the volume of these residues is rather small we consider the effect on NHA properties to be negligible.

## VI. APPLICATION APPROACH AND SENSOR DISCUSSION

While our sensor concept can operate with a fixed-wavelength light source supplied by a laser diode, particularly for low-cost application scenarios it would be advantageous to achieve sensor operation with an LED light source. Since an LED spectrum is broader compared to the spectrum of a laser source, we used our measured sensor responsivities to predict how the photocurrent and therefore the signal of the sensor would change if we used an LED. Since it was not possible to introduce an LED in the Measurement set up, we instead chose the spectral power distribution of a commercial NIR LED (OSA OPTO LIGHT 550/ EOLD [24]) with a centre wavelength of 1300 nm, to calculate the response of the refraction index sensor with an broad light
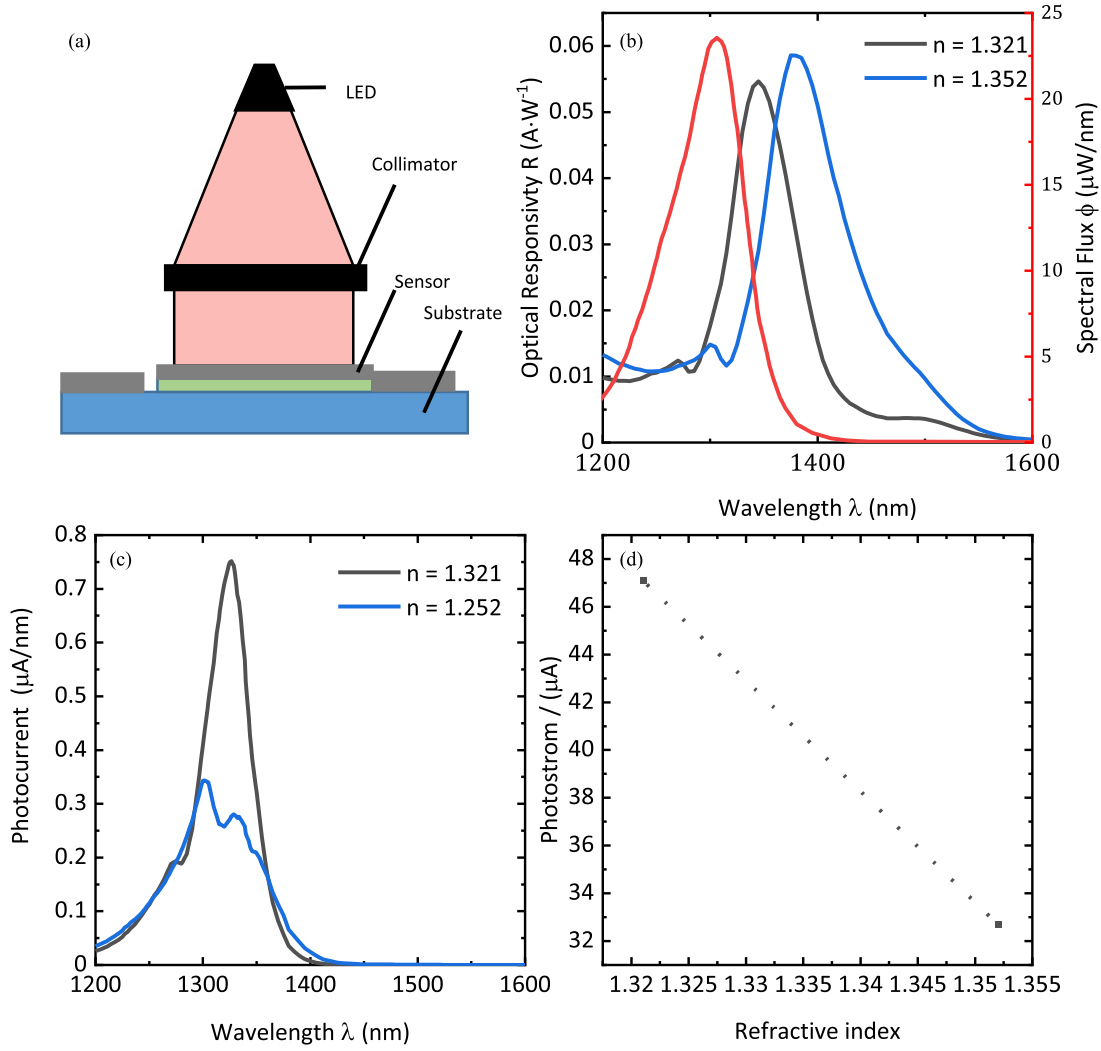
Fig. 8. (a) Schematic setup of the sensor combined with an LED light source. (b) Calculated optical power distribution of the LED and optical responsivity of the sensor. (c) Spectral current distribution of the diode for two different superstrate refraction indices. (d) Calculated change in photocurrent resulting from a superstrate refractive index change.

source. The device has a typical optical power of 2.2 mW at 20 mA. Our application scenario is shown in Fig. 8(a), where we assume an incident angle of 0° achieved by collimation and by bringing the LED in close proximity to our diode. We can estimate the photocurrent generated in the device based on the spectral flux of the LED (Fig. 8(b)) and the responsivity of our sensor. Fig. 8(c) shows the predicted photocurrent spectra obtained in this manner. By changing the refractive index of the superstrate and therefore shifting the responsivity peak from 1345 nm to 1375 nm, we see that the spectral photocurrent distribution that we can expect to obtain from our device changes strongly. Integrating over all wavelengths allows us to predict the total expected photocurrent for the two refractive indices corresponding to DI water and ethanol. For DI-water the predicted photocurrent signal is $I = 47.1$ $\mu$A and for ethanol we obtain $I = 32.7$ $\mu$A. Given the fact that a superstrate refractive index change results in a proportional shift of the device responsivity spectrum [25] and taking into account the shape of the LED spectrum (Fig. 8(b)), we can postulate a linear dependence of

the photocurrent on the refractive index also for intermediate values of the refractive index, with a predicted slope of $\Delta I = -466$ $\mu$A/RIU as seen in Fig. 8(d). Since the sensor is operated at 0 V bias, the dark current and therefore the current resolution limit is set by the read out electronic, Fig. 9 shows the dark current. The measured dark current at 0 V external bias was at around 10 nA, which could be improved using fully integrated readout electronics [26], [27]. If we assume the fluctuation of the dark current over time to be at least on order of magnitude smaller than the dark current itself, the signal to noise ratio should be high enough to detect a signal change of 10 nA in the photocurrent. This corresponds to a change in refractive index of $2.2 \cdot 10^{-5}$, which is equivalent to an ethanol concentration of 1% in DI water.

## VII. Summary

The integration of plasmonic nanostructures with vertical Ge-on-Si PIN photodiodes has tremendous potential for application
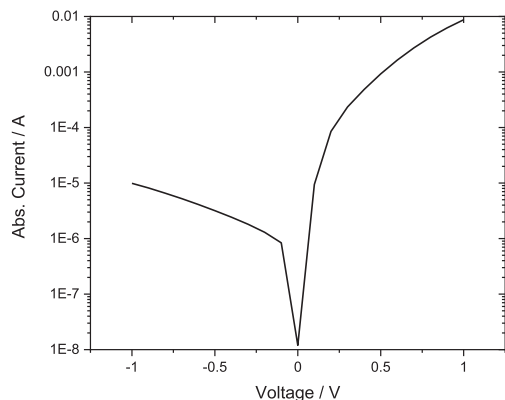
Fig. 9.    Dark current of the measured Ge-PIN photodiode.

in refractive index sensing if the device performance can be tuned. Here, we present a device optimization approach for two different application scenarios. Our simulation results show that by iteratively optimizing the photodiode layer stack as well as the geometry of the nanohole-array on top of the Ge-on-Si PIN photodiode it is possible to obtain sharp Fano resonances in the responsivity of the devices that are well suited for the detection of refractive index changes. With our simulative optimization approach, it is possible to optimize the sensor for any refractive index and wavelength combination. The device performance of the fabricated devices shows a clear improvement over previous results concerning the signal width and FOM∗. Furthermore, we predict that the narrow resonances of the fabricated devices enable the use of a LED as a light source for a cost-effective sensor setup that can detect refractive index changes via changes in the total photocurrent with a slope of $\Delta I = -466\ \mu$A/RIU. This can be utilized to design and create fully integrated refractive index sensors and biosensors. Our fabricated devices also show that further device improvements require a reduction of fabrication inaccuracies. If these issues can be addressed, it should be possible to achieve even higher responsivities and to improve the agreement between experimental results and simulated device characteristics. This work, thus, constitutes a further step towards the development of fully integrated plasmonic biosensors.

## References

[1] A. G. Brolo, "Plasmonics for future biosensors," *Nature Photon.*, vol. 6, no. 11, pp. 709–713, 2012, doi: 10.1038/nphoton.2012.266.

[2] V. Owen, "Real-time optical immunosensors — A commercial reality," *Biosensors Bioelectron.*, vol. 12, no. 1, pp. 1–2, 1997, doi: 10.1016/0956-5663(96)89090-7.

[3] B. Liedberg, C. Nylander, and I. Lunström, "Surface plasmon resonance for gas detection and biosensing," *Sensors Actuators*, vol. 4, pp. 299–304, 1983, doi: 10.1016/0250-6874(83)85036-7.

[4] Carlos Escobedo, "On-chip nanohole array based sensing: A review," *Lab Chip*, vol. 13, no. 13, pp. 2445–2463, 2013, doi: 10.1039/C3LC50107H.

[5] L. Li *et al.*, "Gap-mode excitation, manipulation, and refractive-index sensing application by gold nanocube arrays," *Nanoscale*, vol. 11, no. 12, pp. 5467–5473, 2019, doi: 10.1039/C8NR09073D.

[6] F. Mazzotta, G. Wang, C. Hägglund, F. Höök, and M. P. Jonsson, "Nanoplasmonic biosensing with on-chip electrical detection," *Biosensors Bioelectron.*, vol. 26, no. 4, pp. 1131–1136, Dec. 2010, doi: 10.1016/j.bios.2010.07.008.

[7] L. Guyot, A.-P. Blanchard-Dionne, S. Patskovsky, and M. Meunier, "Integrated silicon-based nanoplasmonic sensor," *Opt. Exp.*, vol. 19, no. 10, pp. 9962–9967, 2011, doi: 10.1364/OE.19.009962.

[8] S. Patskovsky and M. Meunier, "Integrated Si-based nanoplasmonic sensor with phase-sensitive angular interrogation," *Annalen Der Physik*, vol. 525, no. 6, pp. 431–436, 2013, doi: 10.1002/andp.201300078.

[9] I. A. Fischer *et al.*, "Ge-on-Si PIN-photodetectors with al nanoantennas: The effect of nanoantenna size on light scattering into waveguide modes," *Appl. Phys. Lett.*, vol. 108, no. 7, 2016, Art. no. 071108, doi: 10.1063/1.4942393.

[10] R. T. Hill, "Plasmonic biosensors," *Wiley Interdiscipl. Rev.: Nanomedicine Nanobiotechnology*, vol. 7, no. 2, pp. 152–168, 2015, doi: 10.1002/wnan.1314.

[11] L. Augel, S. Bechler, R. Korner, M. Oehme, J. Schulze, and I. A. Fischer, "An integrated plasmonic refractive index sensor: Al nanohole arrays on Ge PIN photodiodes," in *Proc. IEEE Int. Electron Devices Meeting*, 2017, pp. 40.5.1–40.5.4.

[12] L. Augel *et al.*, "Optofluidic sensor system with Ge PIN photodetector for CMOS-compatible sensing," *Microfluidics Nanofluidics*, vol. 21, no. 11, 2017, Art. no. 169, doi: 10.1007/s10404-017-2007-3.

[13] L. Augel *et al.*, "Integrated collinear refractive index sensor with Ge PIN photodiodes," *ACS Photon.*, vol. 5, no. 11, pp. 4586–4593, 2018, doi: 10.1021/acsphotonics.8b01067.

[14] Lumerical Inc., FDTD: 3D Electromagnetic Simulator, [Online]. Available: https://www.lumerical.com/products/

[15] Y. Kawaguchi, L. Augel, H. Uchida, M. Inoue, J. Schulze, and I. A. Fischer, "Simulation-based optimization of Ge-PIN-photodiodes with al nanohole arrays for refractive index sensing," in *Proc. 41st Int. Conv. Inf. Commun. Technol., Electron. Microelectronics*, 2018, pp. 23–26.

[16] J. Becker, A. Trügler, A. Jakab, U. Hohenester, and C. Sönnichsen, "The optimal aspect ratio of gold nanorods for plasmonic Bio-sensing," *Plasmonics*, vol. 5, no. 2, pp. 161–167, 2010, doi: 10.1007/s11468-010-9130-2.

[17] P. Lovera, D. Jones, B. Corbett, and A. O'Riordan, "Polarization tunable transmission through plasmonic arrays of elliptical nanopores," *Opt. Exp.*, vol. 20, no. 23, pp. 25325–25332, 2012, doi: 10.1364/OE.20.025325.

[18] S. Kedenburg, M. Vieweg, T. Gissibl, and H. Giessen, "Linear refractive index and absorption measurements of nonlinear optical liquids in the visible and near-infrared spectral region," *Opt. Mater. Exp.*, vol. 2, no. 11, pp. 1588–1611, 2012, doi: 10.1364/OME.2.001588.

[19] E. Sani and A. Dell'Oro, "Spectral optical constants of ethanol and isopropanol from ultraviolet to far infrared," *Opt. Mater.*, vol. 60, no. 35, pp. 137–141, 2016, doi: 10.1016/j.optmat.2016.06.041.

[20] R. Farzana *et al.*, "3D OCT characterization and quantification of refractive indices of bacteria and biofilms with antibiotic interventions," in *Proc. Opt. Mol. Probes, Imag. Drug Del.*, 2021, doi: 10.1364/OMP.2021.OTu3D.5.

[21] R. Bakke, R. Kommedal, and S. Kalvenes, "Quantification of biofilm accumulation by an optical approach," *J. Microbiological Methods*, vol. 44, no. 1, pp. 13–26, 2001, doi: 10.1016/S0167-7012(00)00236-0.

[22] A. E. Cetin *et al.*, "Handheld high-throughput plasmonic biosensor using computational on-chip imaging," *Light Sci. Appl.*, vol. 3, no. 1, 2014, Art. no. e122, doi: 10.1038/lsa.2014.3.

[23] M. Vala, C. T. Ertsgaard, N. J. Wittenberg, and S.-H. Oh, "Plasmonic sensing on symmetric nanohole arrays supporting high-Q hybrid modes and reflection geometry," *ACS Sens.*, vol. 4, no. 12, pp. 3265–3274, 2019, doi: 10.1021/acssensors.9b01780.

[24] OSA Opto Light GmbH, *Data sheet: Infrared LED EOLD-1300-525*. [Online]. Available: https://www.osa-opto.com/smd-leds/eold-1300-525.html

[25] L. Qin, S. Wu, J.-H. Deng, L. Li, and X. Li, "Tunable light absorbance by exciting the plasmonic gap mode for refractive index sensing," *Opt. Lett.*, vol. 43, no. 7, pp. 1427–1430, 2018, doi: 10.1364/OL.43.001427.

[26] D. Djekic, G. Fantner, J. Behrends, K. Lips, M. Ortmanns, and J. Anders, "A transimpedance amplifier using a widely tunable PVT-independent pseudo-resistor for high-performance current sensing applications," in *Proc. 43rd IEEE Eur. Solid State Circuits Conf.*, 2017, pp. 79–82.

[27] G. Ferrari, F. Gozzini, A. Molari, and M. Sampietro, "Transimpedance amplifier for high sensitivity current measurements on nanodevices," *IEEE J. Solid-State Circuits*, vol. 44, no. 5, pp. 1609–1616, May 2009, doi: 10.1109/JSSC.2009.2016998.